

RESEARCH ARTICLE

10.1029/2019GC008181

Key Points:

- Crustal anisotropy in the central North China Craton is measured at 112 seismic stations using moveout of *P*-to-*S* converted phases
- Significant crustal anisotropy in the Zhangjiakou-Penglai Fault Zone is closely related to the degree of crustal deformation
- Contrasting difference in the fast orientations is revealed between the western and eastern Yanshan Uplifts

Supporting Information:

- Supporting Information S1
- Table S1
- Table S2

Correspondence to:

Z. Ding,
zhfding@vip.sina.com

Citation:

Zheng, T., Ding, Z., Ning, J., Liu, K. H., Gao, S. S., Chang, L., et al. (2019). Crustal azimuthal anisotropy beneath the central North China Craton revealed by receiver functions. *Geochemistry, Geophysics, Geosystems*, 20. <https://doi.org/10.1029/2019GC008181>

Received 4 JAN 2019

Accepted 11 APR 2019

©2019. American Geophysical Union.
All Rights Reserved.

Crustal Azimuthal Anisotropy Beneath the Central North China Craton Revealed by Receiver Functions

Tuo Zheng^{1,2,3,4}, Zhifeng Ding¹, Jieyuan Ning², Kelly H. Liu³, Stephen S. Gao³, Lijun Chang¹, Fansheng Kong^{3,5}, and Xiaoping Fan⁴

¹Institute of Geophysics, China Earthquake Administration, Beijing, China, ²School of Earth and Space Sciences, Peking University, Beijing, China, ³Geology and Geophysics Program, Missouri University of Science and Technology, Rolla, MO, USA, ⁴College of Transportation Science and Engineering, Nanjing Tech University, Nanjing, China, ⁵Key Laboratory of Submarine Geosciences, Second Institute of Oceanography, State Oceanic Administration, Hangzhou, China

Abstract To characterize crustal anisotropy beneath the central North China Craton (CNCC), we apply a recently developed deconvolution approach to effectively remove near-surface reverberations in the receiver functions recorded at 200 broadband seismic stations and subsequently determine the fast orientation and the magnitude of crustal azimuthal anisotropy by fitting the sinusoidal moveout of the *P* to *S* converted phases from the Moho and intracrustal discontinuities. The magnitude of crustal anisotropy is found to range from 0.06 s to 0.54 s, with an average of 0.25 ± 0.08 s. Fault-parallel anisotropy in the seismically active Zhangjiakou-Penglai Fault Zone is significant and could be related to fluid-filled fractures. Historical strong earthquakes mainly occurred in the fault zone segments with significant crustal anisotropy, suggesting that the measured crustal anisotropy is closely related to the degree of crustal deformation. The observed spatial distribution of crustal anisotropy suggests that the northwestern terminus of the fault zone probably ends at about 114°E. Also observed is a sharp contrast in the fast orientations between the western and eastern Yanshan Uplifts separated by the North-South Gravity Lineament. The NW-SE trending anisotropy in the western Yanshan Uplift is attributable to “fossil” crustal anisotropy due to lithospheric extension of the CNCC, while extensional fluid-saturated microcracks induced by regional compressive stress are responsible for the observed ENE-WSW trending anisotropy in the eastern Yanshan Uplift. Comparison of crustal anisotropy measurements and previously determined upper mantle anisotropy implies that the degree of crust-mantle coupling in the CNCC varies spatially.

1. Introduction

The North China Craton (NCC; Figure 1), located in the eastern margin of the Eurasian Plate, is one of the major Archean cratons in the world and the largest cratonic block in China (Carlson et al., 2005; Kusky & Li, 2003). The central NCC (CNCC; Figure 1) is tectonically divided into the western CNCC and the eastern CNCC by the N-S trending Central Orogenic Belt. The western CNCC is generally regarded as a long-term stable cratonic block and lacks significant internal deformation and large earthquakes (Zhao et al., 2001). On the contrary, the eastern CNCC exhibits active seismicity and has undergone significant tectonic reactivation with a sharp decrease in lithospheric thickness from ~200 km in the Archean to 60–80 km at the present (Chen et al., 2008; Griffin et al., 1998; Zhu et al., 2011; Zhu & Zheng, 2009).

The CNCC consists of four major tectonic units: the Yanshan Uplift in the north, Bohai Bay Basin in the east, Taihangshan Uplift in the middle, and Datong Basin in the west (Figure 1). During the late Mesozoic and Cenozoic, most parts of the CNCC underwent significant tectonic activities originated from the subduction of the Palaeo-Pacific Plate in the east and convergence between the NCC and South China Block in the south (Kusky et al., 2007; Ren et al., 2002). The subsidence of the Bohai Bay Basin and uplift of the Taihangshan are generally considered to be related to the NW-SE extension during this period (Ren et al., 2002; Zhu et al., 2012). In contrast, the Yanshan Uplift along the northern margin of the CNCC experienced several phases of N-S directed compressional deformation, which were followed by widespread tectonic extension in the late Mesozoic (Davis et al., 1998). Since the Mesozoic, cratonic destruction and accompanying large-scale structural deformation and widespread magmatic activities occurred in the eastern NCC, probably due to the subduction of the Pacific slab beneath the eastern NCC (Zhu et al., 2011). Dehydration of H_2O -bearing minerals in the subducted slab may have produced aqueous fluids, which could have migrated upwards

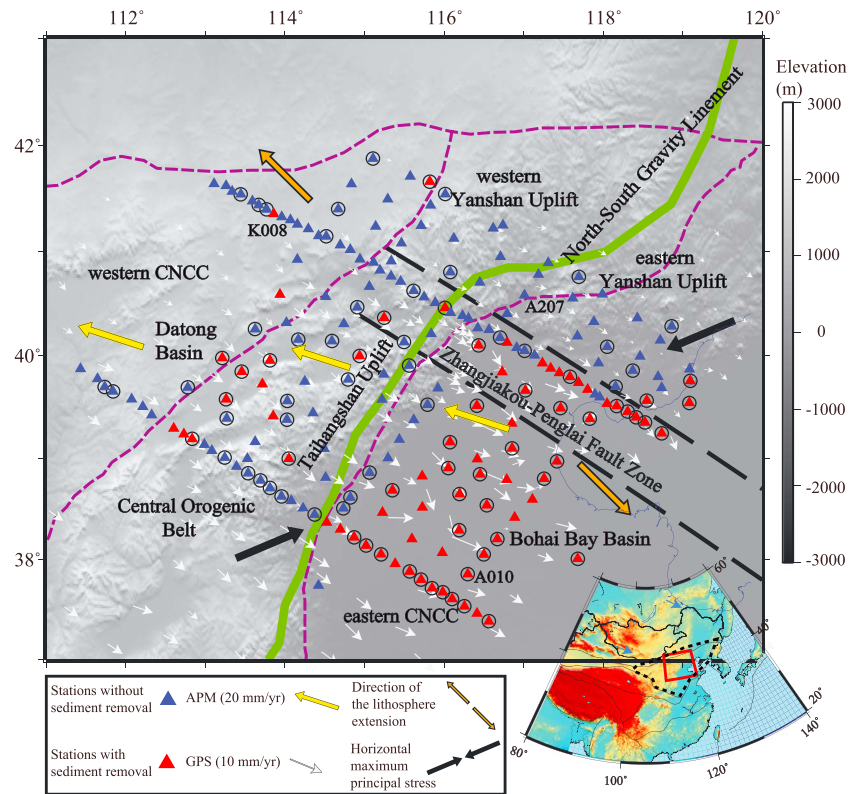


Figure 1. Tectonic background of the study area showing elevation (Amante & Eakins, 2009), major geological block boundaries (dashed purple lines), seismic stations used in the study (triangles), and GPS velocities relative to the stable Eurasian Plate (white arrows; Wang et al., 2001). The red triangles are seismic stations with application of the sediment removal approach (Yu et al., 2015), and the blue triangles are stations without application of the sediment removal approach. Circled stations are not used in the study due to lack of a sufficient number of high-quality receiver functions. The thick green line indicates the North-South Gravity Lineament. The Zhangjiakou-Penglai Fault Zone is approximately outlined by the two black dashed lines. The thick yellow arrows are the Absolute Plate Motion orientations in the HS3-NUVEL-1A model (Gripp & Gordon, 2002). The thick black arrows denote the mean maximum horizontal compressional stress direction (Heidbach et al., 2016). The orange arrows show the orientation of lithospheric extension of the CNCC during the Late Mesozoic and Cenozoic (Ren et al., 2002). The dashed black line in the inset map encloses the NCC, and the red rectangle shows the location of the study area. CNCC = central NCC; NCC = North China Craton.

along the cracks and grain boundaries and hydrated the crust and upper mantle (Iwamori, 2007; Yang et al., 2018a).

The NW-SE trending Zhangjiakou-Penglai Fault Zone (Figure 1) separates the Yanshan and Taihangshan Uplifts and is the boundary zone between the Yanshan Uplift and Bohai Bay Basin (Xu et al., 2002). This sinistral strike slip fault zone (Guo et al., 2015) is seismically the most active region in the CNCC, in which numerous historical destructive earthquakes including the 1976 *M* 7.8 Tangshan earthquake have occurred.

The eastern margin of the Central Orogenic Belt is near the North-South Gravity Lineament (NSGL), a zone of dramatic change in the Bouguer gravity anomaly (e.g., Xu, 2007) and a possible boundary between the area with thinner-than-normal lithosphere to the east and normal lithosphere to the west (Chen et al., 2009). Numerous previous studies have revealed significant differences between the western and eastern sides of the NSGL in crust thickness (Bao et al., 2013; Li et al., 2014; Wu et al., 2018). For example, the crust thickness of the Bohai Bay Basin is about 32 km, while that in the Central Orogenic Belt is 36–40 km (Wu et al., 2018). Lateral variations between the two sides of the NSGL in surface wave phase velocities (Chen et al., 2014), depth of the lithosphere-asthenosphere boundary (Chen et al., 2008), and radial anisotropy (Fu et al., 2015) are also reported. These sharp contrasts in tectonic setting and crustal characteristics, together with the recent availability of a broadband seismic data set recorded by 200 densely spaced stations, make

the CNCC an ideal locale for investigating crustal deformation and its relationship with mantle deformation (e.g., Chen et al., 2009; Gao et al., 2010; Yang et al., 2018b; Zhu et al., 2011).

2. Previous Crustal and Mantle Anisotropy Studies in the CNCC

It has long been recognized that seismic anisotropy can provide important constraints on the deformation and evolution of the lithosphere (e.g., Flesch et al., 2005; Wang et al., 2008). Anisotropy in the upper crust is mostly produced by microcracks (Boness & Zoback, 2006; Crampin & Peacock, 2008; McNamara & Owens, 1993) and that in the lower crust and upper mantle is usually interpreted as strain-induced lattice preferred orientation of anisotropic minerals (Silver, 1996), primarily mica, amphibole, and olivine (Ji et al., 2015; Ko & Jung, 2015).

A number of seismic anisotropy studies, including shear wave splitting (e.g., Bai et al., 2010; Chang et al., 2011, 2012a; Gao et al., 2010; Liu et al., 2008; Zhao & Xue, 2010), surface wave tomography (e.g., Chen et al., 2015; Legendre et al., 2014), and Pn anisotropy tomography (e.g., Zhou & Lei, 2016), have been conducted in the CNCC. Chang et al. (2012a) used SKS splitting to reveal a significant correlation between the fast orientation of upper mantle anisotropy and the absolute plate motion direction in the CNCC and interpreted the correlation by a simple asthenospheric mantle flow. However, most other studies revealed significant variations of fast orientations obtained using one or more of the XKS (including SKS, SKKS, and PKS) phases in different parts of the CNCC (Bai et al., 2010; Liu et al., 2008; Zhao & Xue, 2010). Because anisotropy revealed by the XKS phases can in principle exist from the core mantle boundary to the surface, improving the vertical resolution of anisotropy measurements is key for a realistic interpretation of the observations. While upper crustal anisotropy can be characterized using splitting of direct *S* waves from local earthquakes, one of approaches for the characterization of anisotropy for the entire crust is to utilize source-normalized *P* to *S* converted waves from the Moho ($P_{m,s}$), which are termed as receiver functions (RFs; Kong et al., 2016; Levin & Park, 2000; Liu & Niu, 2012; McNamara & Owens, 1993; Park & Levin, 2016; Rumpker et al., 2014). In the CNCC, Yang et al. (2018b) used a joint analysis (Liu & Niu, 2012) of $P_{m,s}$ waves from RFs to obtain crustal anisotropy measurements at 23 out of 198 stations. They suggested that the observed crustal anisotropy on the margin of the Bohai Bay Basin is related to horizontal principal compressive stress and that in the Yan-shan Uplift indicates an effect of multiple-phase N-S shortening from the early-to-middle Jurassic to the Early Cretaceous. The study also suggested that tectonic extension and magmatic underplating from the Late Mesozoic to Cenozoic may have played a key role in the formation of crustal anisotropy in the Datong Basin. Due to the influence of the thick sedimentary layer (Wu et al., 2018) on the RFs (Yu et al., 2015), no measurements were obtained in the interior part of the Bohai Bay Basin, which occupies a significant portion of the CNCC (Figure 1).

This study takes advantage of a unique data set recorded by a dense portable array and the availability of a recently developed reverberation-removal technique to suppress the influence of the loose sedimentary layer on the RFs (Yu et al., 2015), for the purpose of providing constraints on the formation mechanisms of crustal anisotropy and crust-mantle deformation style in the CNCC, as well as characterizing possible effects of the tectonically active Zhangjiakou-Penglai Fault Zone on crustal anisotropy. Similar to most previous investigations utilizing RFs to quantify crustal anisotropy (e.g., Kong et al., 2016; Liu & Niu, 2012; Nagaya et al., 2008; Rumpker et al., 2014; Sun et al., 2012; Zheng et al., 2018), this study aims at quantifying the bulk crustal anisotropy under the assumption of a single horizontal axis of symmetry and a flat interface.

3. Data and Methods

3.1. Data

The three-component seismic data were recorded by 200 broadband portable stations in the North China Seismic Array (Chen et al., 2014; Wu et al., 2018) deployed between October 2006 and September 2009. Eleven of the stations were equipped with CMG-3T (120 s to 50 Hz) and 189 were equipped with CMG-3ESP sensors (60 s to 50 Hz). The orientation of the sensors was verified by Chang et al. (2012b). The two NW trending profiles (Figure 1) were deployed across the western, central, and eastern CNCC with an interstation distance of about 15 km, and the off-profile stations had an interstation distance of approximately 30 km.

The original RFs used in this study were calculated by Wu et al. (2018) using the following procedure and data processing parameters. Data from a total of 825 teleseismic events with a magnitude M_w greater than

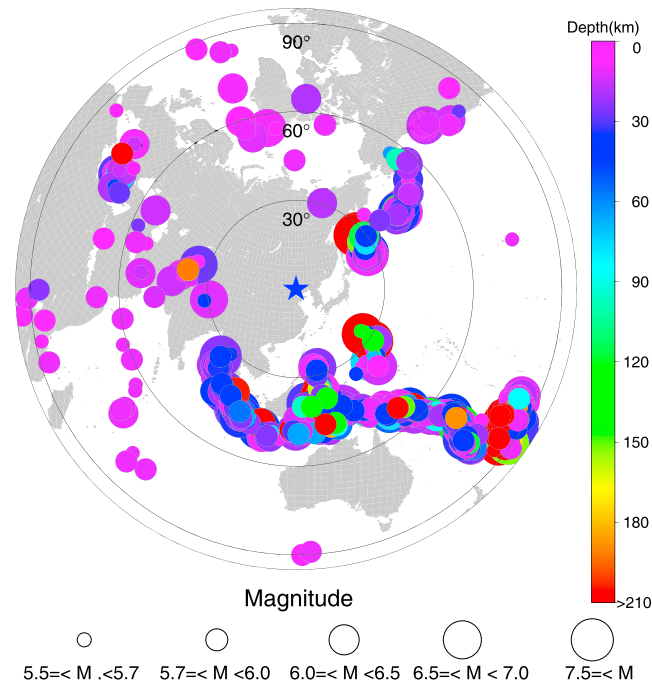


Figure 2. Distribution of teleseismic events used in the study. The circles representing the events are color coded by the focal depths, and the magnitudes are proportional to the size of the circles. The epicentral distances are measured from the center of the study area, which is located at (40.0°N, 116.5°E) and is indicated by the blue star.

5.5 in the epicentral distance range of 30–90° were used for the calculation of P wave RFs. The events have a decent back azimuthal (BAZ) coverage (Figure 2), which is essential for reducing the impact from lateral heterogeneities in the crust and for reliably extracting crustal azimuthal anisotropy measurements. The waveform records were windowed from 10 s before to 150 s after the first P arrival and were filtered in the frequency band of 0.05–2 Hz. The horizontal component seismograms were rotated into the radial and transverse components, and the radial and transverse components were deconvolved from the vertical component using the time domain iterative deconvolution technique (Ligorria & Ammon, 1999) to obtain the RFs (Wu et al., 2018).

To ensure quality, only RFs with an impulsive onset, clear first P arrival, and low-amplitude coda were selected using a signal-to-noise ratio (SNR) based procedure (Gao & Liu, 2014) followed by visual checking. The final data set consists of 57,431 RFs, and the number of RFs per station varies from 17 to 620. While some of the previous crustal anisotropy studies also used the transverse RFs (e.g., Liu & Niu, 2012; Yang et al., 2018b), a visual inspection of the transverse RFs suggests that the arrival corresponding to the Moho on the transverse RFs has a SNR that is much lower than that on the radial RFs (Figure 3). Therefore, only radial RFs are used in the study.

3.2. Removal of Sedimentary Effects on the RFs

The eastern part of the study area is mostly occupied by the Bohai Bay Basin, which is covered by a loose sedimentary layer (Jia et al., 2009; Menzies et al., 2007). Relative to stations on bedrock, the largest arrival of the radial RFs observed at basin stations is the P to S conversion from the base of the sedimentary layer (Yeck et al., 2013; Zelt & Ellis, 1999), and RFs of the basin stations may be contaminated by multiple reverberations generated from the loose sedimentary layer (Tao et al., 2014; Yu et al., 2015), which can mask the P to S conversions from targeted interfaces (Figure 3).

To remove or significantly reduce the influence of the loose sedimentary layer on the crustal anisotropy measurements, we applied a recently developed reverberation removal technique (Yu et al., 2015) to the original RFs provided by Wu et al. (2018). Autocorrelation was performed on the original RFs to obtain the period and strength of the reverberations, which is followed by applying a resonance removal filter in the frequency domain to eliminate or significantly weaken the reverberations. The sediment removal technique is expected to perform well if the reverberations of the resulting RFs are significant, which are indicated

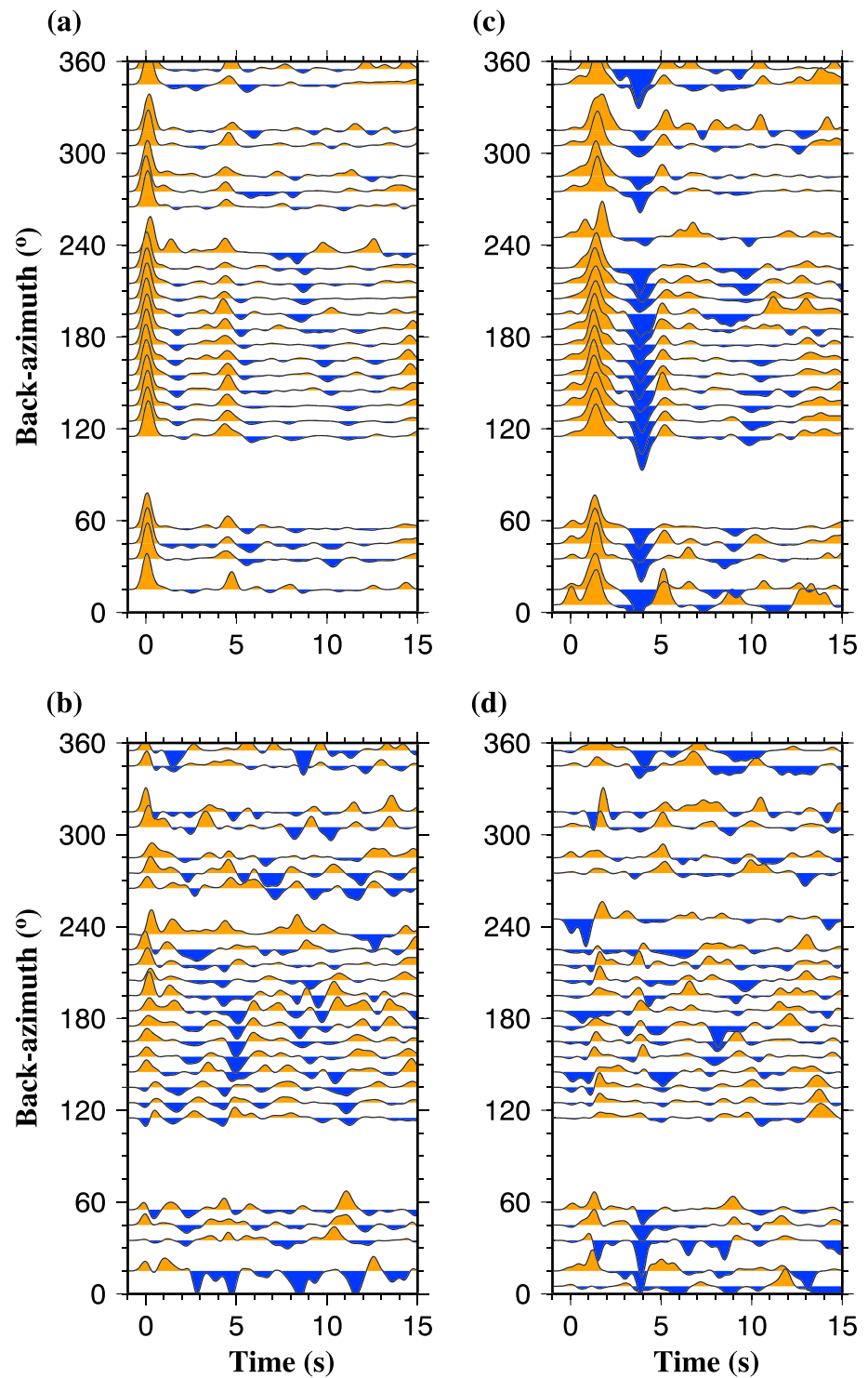


Figure 3. Example RFs plotted against the BAZ. (a) Radial RFs recorded by station A207 (40.58°N, 117.01°E; see Figure 1) situated on bedrock. (b) Transverse RFs recorded by station A207. (c) Radial RFs recorded by basin station A010 (37.86°N, 116.30°E; see Figure 1) located in a sedimentary basin. Note that in (c), the small arrival at time zero is the direct *P* wave, while the largest arrival is the *P* to *S* conversion from the bottom of the sedimentary layer. (d). Transverse RFs recorded by station A010. RF = receiver function.

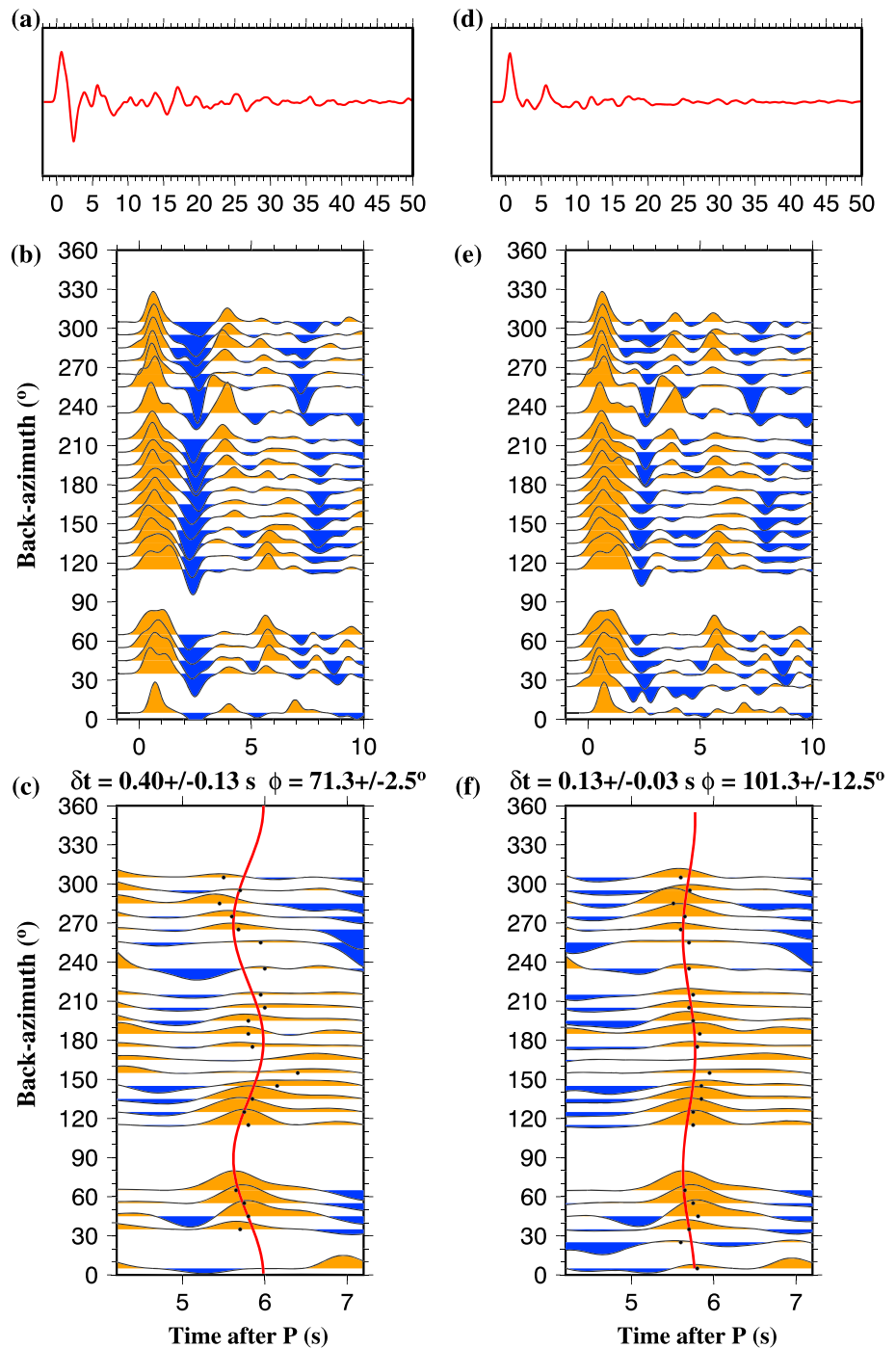


Figure 4. Crustal anisotropy measurements at station K008 (41.36°N, 113.86°E; see Figure 1). (a) The red trace shows the result of simple time domain summation of the individual original radial RFs. (b) BAZ band averaged original radial RFs plotted against the BAZ for the time window of 0–10 s. (c) BAZ band averaged original radial RFs for the time window of 4–7 s. The dot on each of the traces indicates the peak of the P_m s arrival. The red curve is the theoretical P_m s moveout using equation (1). (d–f) The same as (a)–(c) but for RFs after removing the reverberations. RF = receiver function; BAZ = back azimuthal.

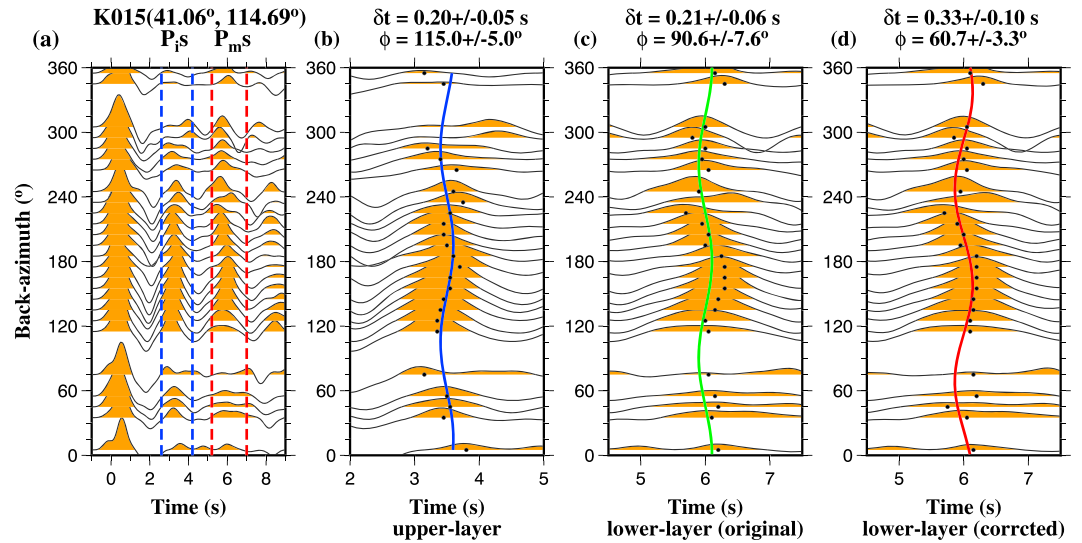


Figure 5. Double-layered crustal anisotropy measurements at station K015 (41.06°N, 114.69°E; see Figure 1). (a) Bin-averaged radial receiver functions plotted against the back azimuthal showing the P_mS (between the two red dashed lines) and P_iS (between the two blue dashed lines) arrivals. (b) Azimuthal variation of the P_iS . The blue curve is the theoretical moveout computed using the optimal anisotropy parameters from the P_iS phase. (c) Azimuthal variation of the P_mS before correcting for anisotropy above the P_iS . The green curve is the theoretical moveout computed using the optimal anisotropy parameters from the P_mS phase. (d) Azimuthal variation of the P_mS after correcting the P_mS parameters with those obtained from the P_iS phase. The resulting anisotropy parameters characterize crustal anisotropy beneath the intracrustal interface.

by a clear sequence of decaying sinusoids and a delayed largest peak, which is the P to S converted phase from the bottom of the loose sedimentary layer (Figure 3c). Among the 200 stations, 76 (Tables S1 and S2) were processed with the reverberation removal technique. The locations of these stations correspond well with the area with a thick sedimentary cover (Figure 1; Wu et al., 2018). An example of crustal anisotropy measurement by using the reverberation-removed RFs can be found in Figure 4.

3.3. Detection of Crustal Azimuthal Anisotropy

When the P to S converted phases travel through an anisotropic layer with a horizontal axis of symmetry, the arrival time (t) can be expressed as (Liu & Niu, 2012; Rumpker et al., 2014)

$$t = t_0 + \Delta t = t_0 - \frac{\delta t}{2} \cos[2(\phi - \theta)], \quad (1)$$

where t_0 is the arrival time of the P to S converted phases in an isotropic crust, Δt denotes the moveout due to crustal anisotropy along the raypath, ϕ is the fast orientation (measured clockwise from the north) along which the P to S converted phases have the earliest arrival and is equivalent to the fast polarization orientation in shear wave splitting analysis, δt is the magnitude of seismic anisotropy and is equivalent to the delay time between the fast and slow shear waves in shear wave splitting analysis, which represents the strength of crustal azimuthal anisotropy, and θ is the BAZ of the RFs.

The following preprocessing steps are conducted for the purpose of increasing the reliability of the measured anisotropy parameters: (1) all the arrival times of the P to S converted phases are corrected to a uniform epicentral distance of 60°; (2) traces within 10° azimuthal bins are stacked together to increase the SNR and eliminate dominance by RFs from a limited number of BAZ bands; (3) stations at which the number of available BAZ bands is less than 12 out of the 36 possible bands, or there is a BAZ coverage gap of 180° or greater, are rejected in the study; (4) the azimuthal variation of Δt is clear, smooth, and coherent. The two phases utilized in this study include P_iS and P_mS . The former is the P to S converted phase from an intracrustal interface for measuring upper crustal anisotropy parameters, and the latter is the P to S converted phase from the Moho for extracting whole crustal anisotropy parameters.

The anisotropy parameters (δt and ϕ) can be obtained by fitting the arrival times of the P to S converted phases relative to the direct P phase based on equation (1) using a nonlinear least squares fitting procedure

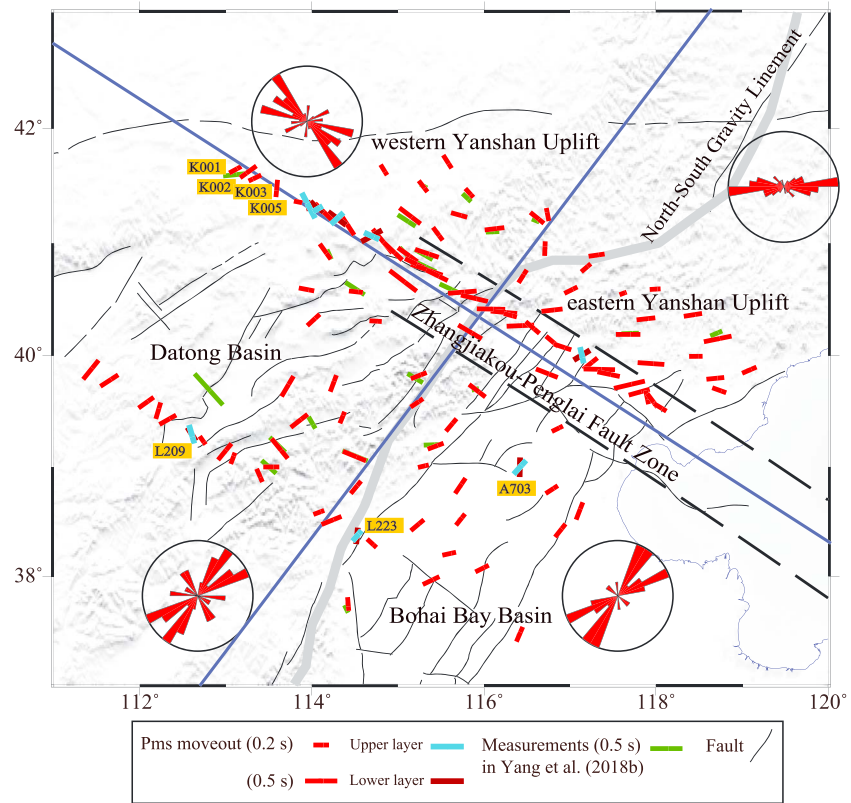


Figure 6. Crustal anisotropy measurements from this study (red bars) and Yang et al. (2018b; green bars). The length and orientation of the bars denote the δt and ϕ measurements, respectively. For the eight stations with double-layered anisotropy, the cyan and brown bars show the upper-layer and lower-layer anisotropy, respectively. The black lines denote active faults at the surface. The blue solid lines separate the study area into four subunits. The equal-area projection rose diagrams represent the distribution of the ϕ values in each of the four subunits.

(Kong et al., 2016). For a few stations where the P_i s can be clearly observed, the layer stripping method (Rumpker et al., 2014) was employed to detect the anisotropy parameters of both the upper and lower layers. In order to obtain reliable double-layered crustal anisotropy measurements, three preconditions are required: (1) the existence of an intracrustal discontinuity; (2) clear and azimuthal variations of P_i s and P_m s arrivals; and (3) good BAZ coverage. Because the P_i s exhibits a characteristic sinusoidal variation with the BAZ, azimuthal anisotropy above the intracrustal interface (“upper crust”) can be detected using the azimuthal moveout of the P_i s phase by applying equation (1). In this case, the arrival times of the P_m s reflect an integrated effect of the two anisotropic layers, and they can be corrected using the resulting upper-layer anisotropy parameters to remove the contribution of the upper layer. The lower-layer parameters can then be determined based on equation (1) to the corrected arrival times of the P_m s (Figure 5).

To evaluate the uncertainties of the resulting crustal anisotropy measurements, we adopt the bootstrap resampling technique (Efron & Tibshirani, 1986; Liu et al., 2003; Liu & Gao, 2010) to measure the mean and standard deviation (SD) of the ϕ and δt of a given station. The resulting SDs after 10 iterations for the two individual parameters are weighted to compute a combined SD for the measurement according to the following equation:

$$\sigma = \frac{\sigma_{\delta t}}{1.0} + \frac{\sigma_{\phi}}{90.0}, \quad (2)$$

where $\sigma_{\delta t}$ is the linear SD for δt , and σ_{ϕ} is the circular SD of ϕ . Stations with a $\sigma \geq 0.4$ are rejected in the study. The application of equation (2) is aimed at normalizing the misfits of the ϕ and δt , which have a maximum angular difference of 90° for ϕ and a maximum difference of 1.0 s for δt .

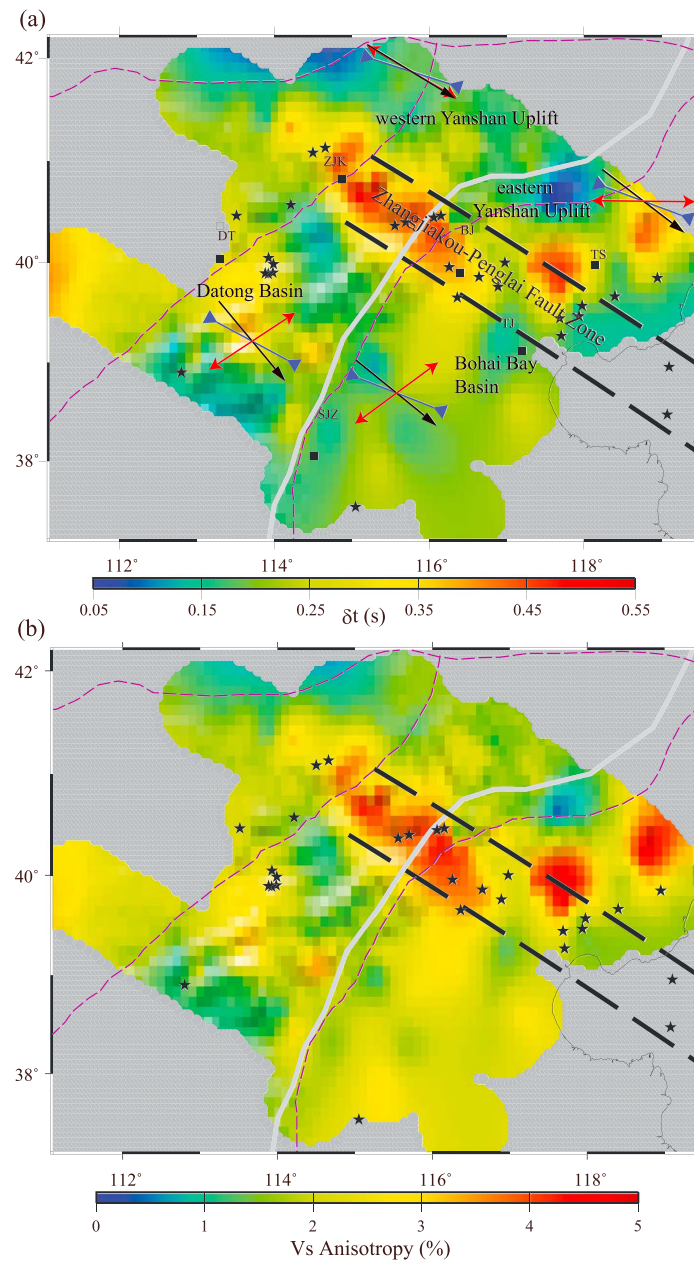


Figure 7. (a) Spatial distributions of the δt measurements. The individual δt observations are fitted using a continuous curvature surface gridding algorithm (Smith & Wessel, 1990) with a tension factor of 0.5 and a sampling interval of 0.1° . The black stars denote $M \geq 6.0$ earthquakes since the 23rd century BCE (Department of Earthquake Disaster Prevention State Seismological Bureau, 1995; Song et al., 2011). The red arrows represent averaged crustal ϕ values in each of the four subunits. The blue arrows show the mean fast orientations from XKS splitting analyses (Bai et al., 2010; Chang et al., 2011, 2012a; Huang et al., 2011; Li et al., 2017; Liu et al., 2008; Zhao & Xue, 2010), and the black arrows are averaged GPS velocities relative to the stable interior of Eurasia (Wang et al., 2001). The black squares mark the locations of cities: Beijing (BJ), Datong (DT), Shijiazhuang (SJZ), Tangshan (TS), Tianjin (TJ), and Zhangjiakou (ZJK). (b) Spatial distributions of the V_s anisotropy using equation (3). This quantity depends on δt , crustal thickness, and crustal V_p/V_s ratio. The average P velocity in the crust is set as 6.1 km/s.

Table 1

Averaged Anisotropy Parameters From Direct S Splitting in the Upper Crust (Gao et al., 2010, 2011; Zhao et al., 2011), P_m s Moveout, XKS Splitting (Bai et al., 2010; Chang et al., 2011, 2012a; Huang et al., 2011; Li et al., 2017; Liu et al., 2008; Zhao & Xue, 2010), and GPS Directions (Wang et al., 2001) for the Subareas

| Data in the study area | Western Yanshan Uplift | Eastern Yanshan Uplift | Datong Basin | Bohai Bay Basin |
|----------------------------|---------------------------|---------------------------|-----------------|--------------------|
| Direct $S\phi$ (°) | 85.8 ± 16.4 | 85.5 ± 33.1 | 50.8 ± 35.4 | 91.8 ± 41.8 |
| Direct $S\delta t$ (ms/km) | 2.35 ± 1.39 | 3.64 ± 1.40 | 1.83 ± 1.27 | 2.47 ± 0.91 |
| P_m s ϕ (°) | 120.0 ± 26.1 | 90.6 ± 20.2 | 56.6 ± 33.6 | 53.6 ± 25.2 |
| P_m s δt (s) | 0.29 ± 0.09 | 0.27 ± 0.09 | 0.25 ± 0.07 | 0.19 ± 0.04 |
| XKS ϕ (°) | 107.8 ± 9.7 | 110.5 ± 13.5 | 118.2 ± 27.0 | 111.4 ± 9.8 |
| XKS δt (s) | 0.93 ± 0.19 | 0.91 ± 0.20 | 0.92 ± 0.21 | 0.96 ± 0.18 |
| GPS (°) | 121.3 ± 7.4 | 127.5 ± 14.1 | 140.2 ± 9.3 | 129.1 ± 19.7 |

The observed δt can be used to estimate the average crustal V_s anisotropy according to the following equation:

$$A_{V_s} = \frac{\delta t \cdot V_s}{H} = \frac{\delta t \cdot V_p}{H \cdot k}, \quad (3)$$

where A_{V_s} is the average crustal V_s anisotropy, V_p (6.1 km/s) and V_s are the average P velocity and S velocity, respectively, k is the crustal V_p/V_s ratio, and H is the Moho depth based on a published study (Wu et al., 2018).

4. Results

Among the 200 stations (Figure 1), 104 stations have reliable single-layered and 8 stations have double-layered anisotropy parameters (Tables S1 and S2 in the supporting information). Reverberation removal was applied to 28 of the 112 stations. Figure 6 shows all the 112 crustal anisotropy measurements and the comparison between the P_m s moveout results from this study and the results of Yang et al. (2018b). The observed δt measurements at the stations vary from 0.06 to 0.54 s with an average of 0.25 ± 0.08 s. For stations located in the Zhangjiakou-Penglai Fault Zone, the mean δt is 0.40 ± 0.07 s, which is about twice as large as that observed at stations in the other areas (0.23 ± 0.08 s; Figure 7).

The fast orientations demonstrate spatial consistency with surface geological features. To facilitate discussion, the study area is divided into four subunits separated by the NSGL and Zhangjiakou-Penglai Fault Zone: the Datong Basin, Bohai Bay Basin, western Yanshan Uplift, and eastern Yanshan Uplift (Figure 6 and Table 1). In the Datong and Bohai Bay Basins, the fast orientations are dominantly NE-SW, which is consistent with the regional tectonic trend and dominant strike of surface geological features. A contrast of the ϕ measurements is observed between the western and eastern Yanshan Uplifts separated by the NSGL, with NW-SE fast orientations for the western part, and ENE-WSW for the eastern part (Figure 6).

5. Comparison With Previous Crustal Anisotropy Studies

Yang et al. (2018b) used the P_m s phase to map crustal anisotropy in the CNCC beneath 23 stations and obtained an average δt of 0.23 s. Comparison between our measurements and those by Yang et al. (2018b) is shown in Figure 6. While some differences exist at some stations in the Datong Basin, the δt and ϕ measurements in the whole Yanshan Uplift from the two studies are generally consistent. However, the application of the reverberation removal procedure in this study led to better spatial resolution, especially in the Bohai Bay Basin where no measurement was obtained by Yang et al. (2018b). The increased spatial coverage is essential for constraining anisotropy-forming mechanisms and crust-mantle deformation models.

Besides crustal anisotropy investigations using RFs, a number of surface wave and Pn anisotropy tomography studies have been conducted in the CNCC. Chen et al. (2015) determined 3-D azimuthal anisotropy from inversion of Rayleigh wave dispersions. At the depth range of 30–40 km, the NE-SW trending anisotropy in the Datong Basin and NW-SE trending anisotropy in the western Yanshan Uplift are consistent with results

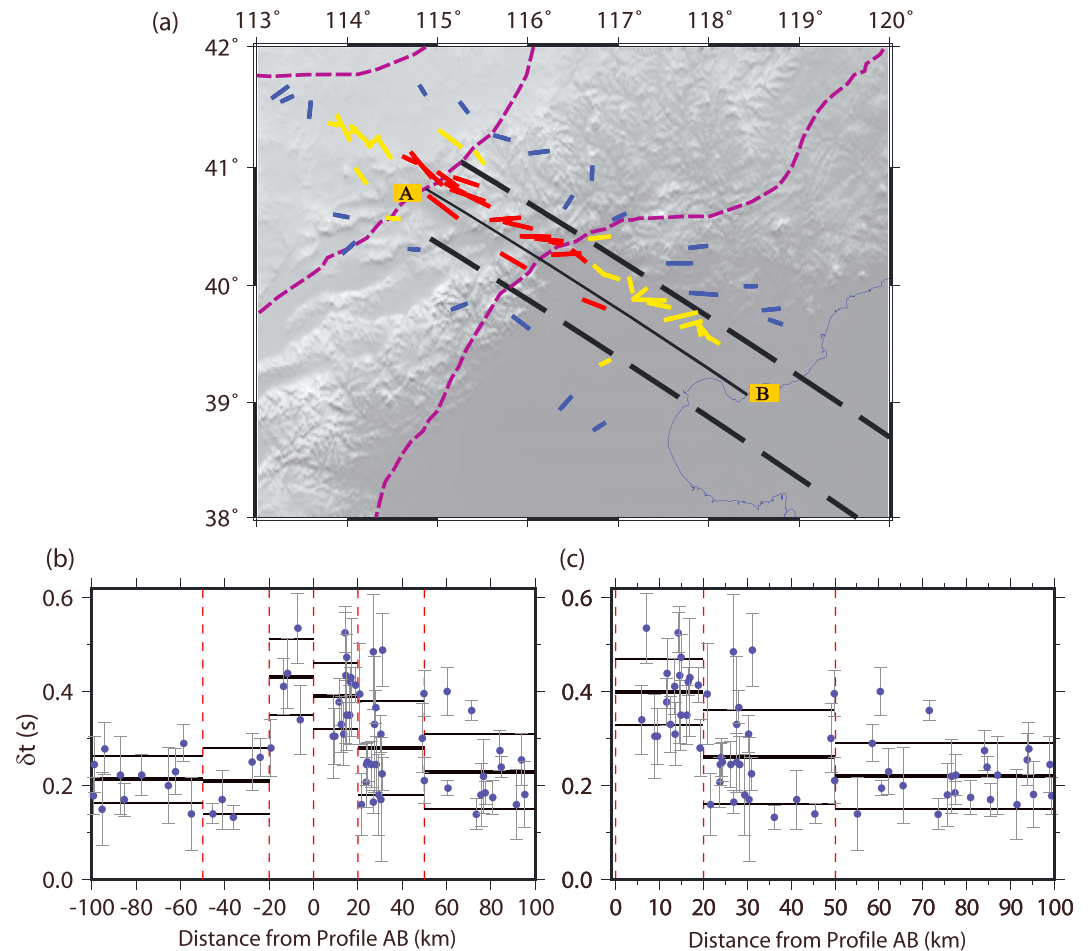


Figure 8. (a) Crustal anisotropy measurements in the Zhangjiakou-Penglai Fault Zone and adjacent areas. Red bars, yellow bars, and blue bars correspond to the measurements that are perpendicular to the center of the fault zone (the solid black line labeled as Profile AB) within 20 km, between 20 and 50 km, and between 50 and 100 km, respectively. The length and orientation of the bars denote the δt and ϕ measurements, respectively. (b) The δt observations (blue dots) at stations that are perpendicular to Profile AB within 100 km. Thick and thin horizontal black bars denote the mean value and standard deviation, respectively. (c) Same as (b) but the observations are plotted against the absolute distance from Profile AB.

from this study. The most significant difference was a nearly 90° deviation of the fast orientations in the eastern Yanshan Uplift. As the crust in the Bohai Bay Basin and eastern Yanshan Uplift is most likely thinner than 40 km (Bao et al., 2013; Li et al., 2014), the azimuthal anisotropy of Rayleigh wave at 40 km may not reflect crustal but mantle anisotropy. Zhou and Lei (2016) presented a high-resolution Pn anisotropic tomography beneath China using arrival time data. The fast orientations from this study agree well with the Pn anisotropy results in most of the study area (Figure 8 in Zhou & Lei, 2016).

6. Discussion

6.1. Formation Mechanisms of the Observed Crustal Anisotropy

6.1.1. Zhangjiakou-Penglai Fault Zone

The NW-SE trending Zhangjiakou-Penglai Fault Zone is seismically the most active fault zone in CNCC, where numerous devastating historical earthquakes have occurred (Figure 7; Department of Earthquake Disaster Prevention State Seismological Bureau, 1995; Song et al., 2011). The Zhangjiakou-Penglai Fault Zone is a crustal- or lithospheric-scale fault zone and is a major seismogenic structure in North China (Guo et al., 2015). Microcracks in the middle to lower crust may thus have a significant effect on crustal anisotropy. For stations within 20 km from the center of the fault zone (Profile AB in Figure 8a), the average δt values are similar between the two sides of Profile AB. The average δt of 0.40 ± 0.07 s in the band of 0–20 km from the fault zone is the largest in the three distance bands shown in Figure 8c, suggesting that the crust

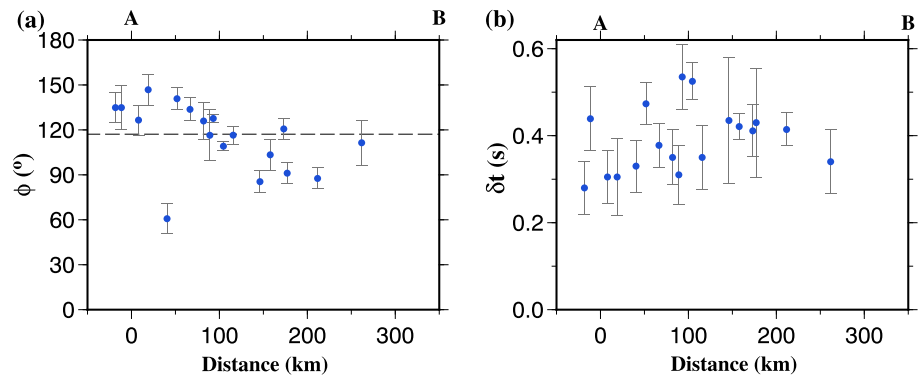


Figure 9. (a) The ϕ measurements observed at stations within 20 km from Profile AB in Figure 8a plotted against the distance from Point A. The dashed black line is the approximate strike of the Zhangjiakou-Penglai Fault Zone. (b) The same as Figure 9a but for the δt observations.

beneath the fault zone is more anisotropic than the areas away from the fault. The large δt measurements also suggest that crustal anisotropy in the fault zone has a nonnegligible contribution to the XKS splitting measurements, which have a δt of about 0.9 s in the area (e.g., Chang et al., 2012a). The zone of anomalously large δt measurements has a total width of about 40 km approximately centered at the fault zone, and the δt measurements show insignificant variations with the distance from the center of the fault zone, which may imply the existence of a broad shear zone at depth beneath the fault zone. For stations more than 20 km away from Profile AB (Figure 8), the average δt values of the two sides are statistically identical (thick horizontal red bars in Figure 8b), and the observed δt measurements demonstrate a gradual decrease with increasing distance from the fault (from 0.40 ± 0.07 s for 0–20 km, to 0.22 ± 0.07 s for 50–100 km). Such a spatial variation is consistent with results from a direct S splitting study (Gao et al., 2011), which shows that the average delay time in the central part of the fault zone is greater than 5 ms/km, whereas that in the area away from the fault is generally less than 3 ms/km. The inverse relationship between the δt measurements and the distance to the center of the fault zone, when combined with the observation that the fast orientations at the stations closest to the fault zone are parallel or subparallel to the strike of the fault zone (Figure 9), may indicate a gradual intensification of fluid-filled fractures toward the center of the active fault zone (Kong et al., 2016; Zheng et al., 2018). An alternative mechanism for the enhanced anisotropy along the fault zone is a broad zone of viscous deformation in the middle to lower crust, and a narrow zone of fluid-filled fractures in the upper crust (e.g., Burgmann & Dresen, 2008). However, this mechanism is not in good agreement with the presence of earthquakes in the middle and lower crust along the fault zone (Guo et al., 2015), which suggests brittle rather than ductile deformation dominates in the middle and lower crust.

Three stations (stations L209, L223, and A703 in Figure 6) located far away from the Zhangjiakou-Penglai Fault Zone show double-layered anisotropy. For all the three stations, the fast orientations for the upper and lower layers are similar. In contrast, the fast orientations for the upper and lower layers measured at five stations in the Zhangjiakou-Penglai Fault Zone are significantly different (Figure 6). This nearly 90° flip of the fast orientations is also found by direct S splitting from local events conducted in the Zhangjiakou-Penglai Fault Zone (Gao et al., 2011) and active fault zones in Iceland (Crampin et al., 2002), as well as P_m s moveout in the eastern Tibetan Plateau (Kong et al., 2016; Zheng et al., 2018). The 90° difference between the fast orientation of the upper and lower layers could be caused by complex crustal structure beneath the fault zone with a broad shear zone at depth. Alternatively, a 90° flip in the fast orientation is expected if the pore pressure exceeds the maximum horizontal compression stress (Crampin et al., 2002; Gao et al., 2011).

The observed spatial distribution of crustal anisotropy can be used to provide constraints on the location of the northwestern terminus of the Zhangjiakou-Penglai Fault Zone, which has been a debated issue (Guo et al., 2015; Ju et al., 2016; Suo et al., 2013). The fast orientations at stations K001-K003 and K005 (Figure 6) are inconsistent with the strike of the Zhangjiakou-Penglai Fault Zone, and the δt measurements are smaller than those observed in the fault zone, suggesting that the fault zone most probably ends at about 114°E (Figure 6).

6.1.2. Different Anisotropy-Forming Mechanisms Between the Western and Eastern Yanshan Uplifts

The western and eastern Yanshan Uplifts are separated by the NSGL, and significant differences in crustal and mantle velocity structure between the western and eastern Yanshan Uplifts are found by previous studies. An *S*-RF study (Chen et al., 2008) suggested the presence of a shallower lithosphere-asthenosphere boundary beneath the eastern Yanshan Uplift than the western Yanshan Uplift. The Moho depth also decreases from west to east (Jia et al., 2009; Li et al., 2014). Surface wave phase velocity tomography (Chen et al., 2014, 2015) and ambient noise tomography investigations (Bao et al., 2013) revealed that relative to the western part, the eastern Yanshan Uplift has a lower velocity structure from the middle and lower crust to the upper mantle.

Our measurements show a clear contrast in the fast orientations between the western and eastern Yanshan Uplifts (Figure 6). The measured fast orientations in the western Yanshan Uplift are consistent with the NW-SE trending lithospheric extensional stress field of the CNCC during the Late Mesozoic and Cenozoic (Ren et al., 2002). The extensional stress is also consistent with the strong positive radial anisotropy ($V_{SH} > V_{SV}$) observed in the western Yanshan Uplift from 25-km depth to the Moho (Figure 9f in Fu et al., 2015). In addition, both surface wave and body wave tomography investigations revealed pronounced high-velocity continental roots beneath the western CNCC including the western Yanshan Uplift (An & Shi, 2006; Huang & Zhao, 2006; Li et al., 2006). Chang et al. (2012a) used XKS splitting measurements to suggest that the average delay time in the western CNCC is about 0.75 s, which is less than the global average of 1 s (Silver, 1996) but is comparable to the splitting times observed beneath other major stable cratons such as those found in Craton in southern Africa (Silver et al., 2001) and North America (Liu et al., 2014). We speculate that the NW-SE trending crustal anisotropy in the western Yanshan Uplift is possibly part of the “fossil” anisotropy frozen in the thick lithosphere due to lithospheric extension of the CNCC.

Contrary to the western Yanshan Uplift, the fast orientations observed in the eastern Yanshan Uplift are ENE-WSW, which is approximately consistent with the direction of the regional compressive stress (Figures 1 and 6; Heidbach et al., 2016). Although the influence of the Mesozoic-Cenozoic NW-SE extension on crustal anisotropy in this area cannot be readily ruled out, this similarity suggests that extensional fluid-saturated microcracks associated with the regional compression may be responsible for the observed crustal anisotropy. While the resulting ENE-WSW measurements agree well with previous direct *S* splitting results (Gao et al., 2010, 2011), the average delay time in their studies is only about 0.05 s and significantly less than the average value of 0.27 ± 0.09 s found by this study, suggesting the existence of significant anisotropy in the aseismic middle and lower crust.

6.1.3. The Datong and Bohai Bay Basins

Crustal anisotropy observed in the Datong and Bohai Bay Basins is similar, with predominantly NE-SW fast orientations which are basically parallel to the strike of major basement faults as well as the orientation of the maximum compressional stress (Figure 1). Numerous Holocene and late Pleistocene NE trending faults commonly occur in the Datong and Bohai Bay Basins (Figure 6; Ding, 1991). Relocation of small earthquakes in this area suggested that the distribution of the earthquakes is closely related to seismic faults and the focal depth of some earthquakes has even reached the Moho (Zhao et al., 2013), suggesting brittle deformation in the whole crust. Therefore, it is reasonable to hypothesize that the observed crustal anisotropy in the two basins is associated with the active faults and extensional cracks related to the regional compressional stress.

6.2. Crust-Mantle Coupling Relationship

Coupling relationship between the crust and mantle is closely related to past dynamic processes in the lithosphere and is also critically influenced by present-day plate movements (e.g., Bendick & Flesch, 2007; Flesch et al., 2005; Wang et al., 2008). The degree of crust-mantle coupling in the NCC is an important factor in the establishment of the present-day deep dynamic movement model for eastern China (Gao et al., 2010). Because results from GPS, P_m s moveout, and XKS splitting act as a proxy for surface deformation field, crustal deformation field, and upper mantle deformation field, respectively, the three types of measurements can be combined to evaluate the deformation at different depths within the crust and mantle and the extent of crust-mantle coupling (e.g., Flesch et al., 2005; Holt, 2000; Long & Silver, 2009). Good agreements (Figure 7 and Table 1) among the GPS observations, the P_m s moveout, and the XKS splitting in the northwestern CNCC, further imply a coupled crust and mantle deformation model. In contrast, significant discrepancies among the three measurements in the eastern CNCC, together with the significant depth variations of the dominant fast orientations revealed by surface wave tomography (Chen et al., 2015), may

suggest that the crust and mantle are possibly decoupled. Ambient noise tomography study (Bao et al., 2013) revealed that the western CNCC is marked by a high-velocity (perhaps also higher viscosity) structure from the middle and lower crust to the upper mantle, whereas the eastern CNCC is characterized by low velocities (perhaps lower viscosity) compared to the stable western CNCC. The rheological condition thus may be similar to the crust-mantle coupled deformation model (Flesch et al., 2005; Wang et al., 2008) in the western NCC, but such coupling can hardly exist in the eastern CNCC. In addition, previous studies (Ai et al., 2008; Bao et al., 2013) indicated a strong heterogeneity of the lithospheric mantle in the NCC, which provide additional evidence for different lithospheric deformation characteristics between the northwestern CNCC and the eastern CNCC.

6.3. Correlation With Historical Large Earthquakes

Figure 7a shows the spatial distribution of the δt measurements and the historical large earthquakes. The Zhangjiakou-Penglai Fault Zone, where the observed δt measurements are the largest in the study area, is also the seismically most active zone. In addition, previous studies (Chen et al., 2015; Huang & Zhao, 2004) found that the historical large earthquakes in the CNCC more frequently occurred in the transition zone of low- and high-velocity anomalies. We speculate that the observed significant crustal anisotropy in the Zhangjiakou-Penglai Fault Zone is closely related to the degree of crustal deformation which is in turn associated with the historical large earthquakes.

7. Conclusions

In this study, we investigate the crustal azimuthal anisotropy beneath the CNCC using the sinusoidal move-out of P to S converted phases from the Moho and from an intracrustal discontinuity. The results in the Zhangjiakou-Penglai Fault Zone support the existence of a broad shear zone at depth, and the fault zone has limited influence on the interior of the stable western CNCC. The observed crustal azimuthal anisotropy in the Zhangjiakou-Penglai Fault Zone is likely caused by fluid-filled fractures, and significant crustal anisotropy in the fault zone is related to the degree of crustal deformation which is in turn associated with the historical large earthquakes. The resulting ϕ measurements show an obvious difference between the western and eastern Yanshan Uplifts separated by the NSGL. The consistency between the ϕ measurements and the direction of lithospheric extension indicates that the observed crustal anisotropy in the western Yanshan Uplift may be attributed to “fossil” anisotropy frozen in the thick lithosphere due to lithospheric extension of the CNCC, while extensional fluid-saturated microcracks related to the regional compression may result in the measured crustal anisotropy in the eastern Yanshan Uplift and the Datong and Bohai Bay Basins. The observations from the GPS, whole crust and upper mantle anisotropy, when combined with results from previous studies, imply that crust and mantle coupling relationship in the northwestern CNCC and eastern CNCC may be different.

References

- Ai, Y., Zheng, T., Xu, W., & Li, Q. (2008). Small scale hot upwelling near the north yellow sea of eastern China. *Geophysical Research Letters*, 35, L20305. <https://doi.org/10.1029/2008GL035269>
- Amante, C., & Eakins, B. W. (2009). ETOPO1 1 Arc-minute global relief model: Procedures, data sources and analysis. NOAA Technical Memorandum NESDIS NGDC-24, 19. <https://doi.org/10.7289/V5C8276M>
- An, M. J., & Shi, Y. L. (2006). Lithospheric thickness of the Chinese continent. *Physics of the Earth and Planetary Interiors*, 159(3-4), 257–266. <https://doi.org/10.1016/j.pepi.2006.08.002>
- Bai, L., Kawakatsu, H., & Morita, Y. (2010). Two anisotropic layers in central orogenic belt of North China Craton. *Tectonophysics*, 494, 138–148. <https://doi.org/10.1016/j.tecto.2010.09.002>
- Bao, X., Song, X., Xu, M., Wang, L., Sun, X., Mi, N., et al. (2013). Crust and upper mantle structure of the North China Craton and the NE Tibetan Plateau and its tectonic implications. *Earth and Planetary Science Letters*, 369–370, 129–137. <https://doi.org/10.1016/j.epsl.2013.03.015>
- Bendick, R., & Flesch, L. (2007). Reconciling lithospheric deformation and lower crustal flow beneath central Tibet. *Geology*, 35(10), 895–898. <https://doi.org/10.1130/G23714A.1>
- Boness, N. L., & Zoback, M. D. (2006). Mapping stress and structurally controlled crustal shear velocity anisotropy in California. *Geology*, 34(10), 825–828. <https://doi.org/10.1130/G22309.1>
- Burgmann, R., & Dresen, G. (2008). Rheology of the lower crust and upper mantle: Evidence from rock mechanics, geodesy, and field observations. *Annual Review of Earth and Planetary Sciences*, 36(1), 531–567. <https://doi.org/10.1146/annurev.earth.36.031207.124326>
- Carlson, R. W., Pearson, D. G., & James, D. E. (2005). Physical, chemical, and chronological characteristics of continental mantle. *Reviews of Geophysics*, 43, RG000156. <https://doi.org/10.1029/2004RG000156>
- Chang, L. J., Wang, C.-Y., & Ding, Z. F. (2011). Upper mantle anisotropy in the Ordos Block and its margins. *Science in China Series D: Earth Sciences*, 54, 888–900. <https://doi.org/10.1007/s11430-010-4137-2>

Acknowledgments

The waveform data were provided by the Data Management Center of China National Seismic Network at Institute of Geophysics, China Earthquake Administration (<http://www.seisdmc.ac.cn>). All the receiver function waveforms prior to the application of the reverberation removal technique in Seismic Analysis Codes (SAC) format used in the study can be accessed from <https://zenodo.org/record/2595817> website. Critical reviews by two anonymous reviewers and Editor M. Long significantly improved the manuscript. We thank X. Wang and Y. Wu for calculating the original RFs used in this study. This work is supported by the National Key Research and Development Program of China (grant 2017FYC1500200 to Z. D.), the Special Fund of the Institute of Geophysics, China Earthquake Administration (grant DQJB17A01 to Z. D.), the National Natural Science Foundation of China (grants 41774061 and 41474088 to L. C., and 41874051 to X. F.), the China Scholarship Council to T. Z., and the U.S. National Science Foundation (grants 0911346, 1321656, and 1830644 to K. L. and S. G.).

- Chang, L. J., Wang, C.-Y., & Ding, Z. F. (2012a). Upper mantle anisotropy beneath north China from shear wave splitting measurements. *Tectonophysics*, 522-523(3), 235–242. <https://doi.org/10.1016/j.tecto.2011.12.009>
- Chang, L. J., Wang, C.-Y., & Ding, Z. F. (2012b). Upper mantle anisotropy beneath north China (in Chinese). *Chinese Journal of Geophysics*, 55(3), 886–896. <https://doi.org/10.6038/j.issn.0001-5733.2012.03.018>
- Chen, L., Cheng, C., & Wei, Z. G. (2009). Seismic evidence for significant lateral variations in lithospheric thickness beneath the central and western North China Craton. *Earth and Planetary Science Letters*, 286, 171–183. <https://doi.org/10.1016/j.epsl.2009.06.022>
- Chen, L., Tao, W., Zhao, L., & Zheng, T. (2008). Distinct lateral variation of lithospheric thickness in the northeastern North China Craton. *Earth and Planetary Science Letters*, 267, 56–68. <https://doi.org/10.1016/j.epsl.2007.11.024>
- Chen, H. P., Zhu, L. B., Wang, Q. D., Zhang, P., & Yang, Y. H. (2014). S-wave velocity structure of the north China from inversion of rayleigh wave phase velocity. *Journal of Asian Earth Sciences*, 88, 178–191. <https://doi.org/10.1016/j.jseae.2014.03.006>
- Chen, H. P., Zhu, L. B., Ye, Q. D., Wang, Q. D., Yang, Y. H., & Zhang, P. (2015). Azimuthal anisotropy of the crust and uppermost mantle in northeast North China Craton from inversion of rayleigh wave phase velocity. *Geophysical Journal International*, 202, 624–639. <https://doi.org/10.1093/gji/ggv153>
- Crampin, S., & Peacock, S. (2008). A review of the current understanding of seismic shear-wave splitting in the earth's crust and common fallacies in interpretation. *Wave Motion*, 45(6), 675–722. <https://doi.org/10.1016/j.wavemoti.2008.01.003>
- Crampin, S., Volti, T., Chastin, S., Gudmundsson, A., & Stefansson, R. (2002). Indication of high pore-fluid pressures in a seismically-active fault zone. *Geophysical Journal International*, 151, F1–F5. <https://doi.org/10.1046/j.1365-246X.2002.01830.x>
- Davis, G. A., Wang, C., Zheng, Y., Zhang, J., Zhang, C., & Gehrels, G. E. (1998). The enigmatic Yinshan fold-and-thrust belt of northern China: New views on its intraplate contractional styles. *Geology*, 26(1), 43–46. [https://doi.org/10.1130/0091-7613\(1998\)026<0043:TEYFAT>2.3.CO;2](https://doi.org/10.1130/0091-7613(1998)026<0043:TEYFAT>2.3.CO;2)
- Department of Earthquake Disaster Prevention State Seismological Bureau (1995). Catalogue of Chinese Historical Strong Earthquakes (23th Century BC - 1911 AD) (in Chinese) (pp. 475–479). Beijing: Seismological Press.
- Ding, G. Y. (1991). Lithospheric dynamics of China (in Chinese). *Explanatory Notes for the Atlas of Lithospheric Dynamics of China*. Beijing: Seismological Press.
- Efron, B., & Tibshirani, R. (1986). Bootstrap methods for standard errors, confidence intervals, and other measures of statistical accuracy. *Statistical Science*, 1(1), 54–75. <https://doi.org/10.1214/ss/1177013815>
- Flesch, L. M., Holt, W. E., Silver, P. G., Stephenson, M., Wang, C.-Y., & Chan, W. W. (2005). Constraining the extent of crust-mantle coupling in central Asia using GPS, geologic, and shear wave splitting data. *Earth and Planetary Science Letters*, 238(1-2), 248–268. <https://doi.org/10.1016/j.epsl.2005.06.023>
- Fu, Y. V., Gao, Y., Li, A., & Shi, Y. (2015). Lithospheric shear wave velocity and radial anisotropy beneath the northern part of north China from surface wave dispersion analysis. *Geochemistry Geophysics Geosystems*, 16, 2619–2636. <https://doi.org/10.1002/2015GC005825>
- Gao, S. S., & Liu, K. H. (2014). Mantle transition zone discontinuities beneath the contiguous United States. *Journal of Geophysical Research: Solid Earth*, 119, 6452–6468. <https://doi.org/10.1002/2014JB011253>
- Gao, Y., Wu, J., Fukao, Y., Shi, Y. T., & Zhu, A. L. (2011). Shear wave splitting in the crust in north China: Stress, faults and tectonic implications. *Geophysical Journal International*, 187, 642–654. <https://doi.org/10.1111/j.1365-246X.2011.05200.x>
- Gao, Y., Wu, J., Yi, G. X., & Shi, Y. T. (2010). Crust-mantle coupling in north China: Preliminary analysis from seismic anisotropy. *Chinese Science Bulletin*, 55(31), 3599–3605. <https://doi.org/10.1007/s11434-010-4135-y>
- Griffin, W. L., Zhang, A. D., O'Reilly, S. Y., & Ryan, C. G. (1998). Phanerozoic evolution of the lithosphere beneath the Sino-Korean craton. Mantle dynamics and plate interactions in east Asia. *American Geophysical Union*, 27, 107–126. <https://doi.org/10.1029/GD027p0107>
- Gripp, A. E., & Gordon, R. G. (2002). Young tracks of hotspots and current plate velocities. *Geophysical Journal International*, 150(2), 321–361. <https://doi.org/10.1046/j.1365-246X.2002.01627.x>
- Guo, L. L., Li, S. Z., Suo, Y. H., Ji, Y. T., Dai, L. M., Yu, S., et al. (2015). Experimental study and active tectonics on the Zhangjiakou-Penglai fault zone across north China. *Journal of Asian Earth Sciences*, 114, 18–27. <https://doi.org/10.1016/j.jseae.2015.03.045>
- Heidbach, O., Rajabi, M., Reiter, K., Ziegler, M., & Team, W. (2016). World stress map database release 2016 GFZ Data Services. <https://doi.org/10.5880/WSM.2016.001>
- Holt, W. E. (2000). Correlated crust and mantle strain fields in Tibet. *Geology*, 28, 67–70.
- Huang, Z. C., Wang, L. S., Zhao, D. P., Mi, N., & Xu, M. (2011). Seismic anisotropy and mantle dynamics beneath China. *Earth and Planetary Science Letters*, 306(1-2), 105–117. <https://doi.org/10.1016/j.epsl.2011.03.038>
- Huang, J., & Zhao, D. P. (2004). Crustal heterogeneity and seismotectonics of the region around Beijing, China. *Tectonophysics*, 385, 159–180. <https://doi.org/10.1016/j.tecto.2004.04.024>
- Huang, J., & Zhao, D. P. (2006). High-resolution mantle tomography of China and surrounding regions. *Journal of Geophysical Research*, 111, B09305. <https://doi.org/10.1029/2005JB004066>
- Iwamori, H. (2007). Transportation of h_2O beneath the Japan arcs and its implications for global water circulation. *Chemical Geology*, 239, 182–198. <https://doi.org/10.1016/j.chemgeo.2006.08.011>
- Ji, S., Shao, T., Michibayashi, K., Oya, S., Satsukawa, T., Wang, Q., et al. (2015). Magnitude and symmetry of seismic anisotropy in mica- and amphibole-bearing metamorphic rocks and implications for tectonic interpretation of seismic data from the southeast Tibetan Plateau. *Journal of Geophysical Research: Solid Earth*, 120, 6404–6430. <https://doi.org/10.1002/2015JB012209>
- Jia, S. X., Zhang, C. K., Zhao, J. R., Fang, S. M., Liu, Z., & Zhao, J. M. (2009). Crustal structure of the rift-depression basin and Yanshan uplift in the northeast part of north China. *Chinese Journal of Geophysics*, 52(1), 51–63. <https://doi.org/10.1002/cjg2.1326>
- Ju, W., Sun, W., Ma, X., & Jiang, H. (2016). Tectonic stress accumulation in Bohai-Zhangjiakou seismotectonic zone based on 3D visco-elastic modelling. *Journal of Earth System Science*, 125(5), 1021–1031. <https://doi.org/10.1007/s12040-016-0706-x>
- Ko, B., & Jung, H. (2015). Crystal preferred orientation of an amphibole experimentally deformed by simple shear. *Nature Communications*, 6, 6586. <https://doi.org/10.1038/ncomms7586>
- Kong, F., Wu, J., Liu, K. H., & Gao, S. S. (2016). Crustal anisotropy and ductile flow beneath the eastern Tibetan Plateau and adjacent areas. *Earth and Planetary Science Letters*, 442, 72–79. <https://doi.org/10.1016/j.epsl.2016.03.003>
- Kusky, T. M., & Li, J. (2003). Paleoproterozoic tectonic evolution of the North China Craton. *Journal of Asian Earth Sciences*, 22(4), 383–397. [https://doi.org/10.1016/S1367-9120\(03\)00071-3](https://doi.org/10.1016/S1367-9120(03)00071-3)
- Kusky, T. M., Windley, B. F., & Zhai, M. G. (2007). Tectonic evolution of the north China block: From orogen to craton to orogen. *Geological Society, London. Special Publications*, 280, 1–34. <https://doi.org/10.1144/SP280.1>
- Legendre, C. P., Deschamps, F., Zhao, L., Lebedev, S., & Chen, Q. F. (2014). Anisotropic rayleigh wave phase velocity maps of eastern China. *Journal of Geophysical Research: Solid Earth*, 119, 4802–4820. <https://doi.org/10.1002/2013JB010781>
- Levin, V., & Park, J. (2000). Shear zones in the Proterozoic lithosphere of the Arabian Shield and the nature of the Hales discontinuity. *Tectonophysics*, 323(3-4), 131–148. [https://doi.org/10.1016/S0040-1951\(00\)00105-0](https://doi.org/10.1016/S0040-1951(00)00105-0)

- Li, Y. H., Gao, M. T., & Wu, Q. J. (2014). Crustal thickness map of the Chinese mainland from teleseismic receiver functions. *Tectonophysics*, *611*(1), 51–60. <https://doi.org/10.1016/j.tecto.2013.11.019>
- Li, S. L., Guo, Z., & Chen, Y. J. (2017). Complicated 3D mantle flow beneath northeast China from shear wave splitting and its implication for the Cenozoic intraplate volcanism. *Tectonophysics*, *709*, 1–8. <https://doi.org/10.1016/j.tecto.2017.04.015>
- Li, S. L., Mooney, W. D., & Fan, J. (2006). Crustal structure of mainland China from deep seismic sounding data. *Tectonophysics*, *420*, 239–252. <https://doi.org/10.1016/j.tecto.2006.01.026>
- Ligorria, J. P., & Ammon, C. J. (1999). Iterative deconvolution and receiver-function estimation. *Bulletin of the Seismological Society of America*, *89*(5), 1395–1400.
- Liu, K. H., Elsheikh, A., Lemnifi, A., Purevsuren, U., Ray, M., Refayee, H., et al. (2014). A uniform database of teleseismic shear wave splitting measurements for the western and central United States. *Geochemistry Geophysics Geosystems*, *15*, 2075–2085. <https://doi.org/10.1002/2014GC005267>
- Liu, K. H., & Gao, S. S. (2010). Spatial variations of crustal characteristics beneath the Hoggar swell, Algeria, revealed by systematic analyses of receiver functions from a single seismic station. *Geochemistry Geophysics Geosystems*, *11*, Q08011. <https://doi.org/10.1029/2010GC003091>
- Liu, K. H., Gao, S. S., Gao, Y., & Wu, J. (2008). Shear wave splitting and mantle flow associated with the deflected Pacific slab beneath northeast Asia. *Journal of Geophysical Research*, *113*, B01305. <https://doi.org/10.1029/2007JB005178>
- Liu, K. H., Gao, S. S., Silver, P. G., & Zhang, Y. K. (2003). Mantle layering across central South America. *Journal of Geophysical Research*, *108*(B11), 2510. <https://doi.org/10.1029/2002JB002208>
- Liu, H., & Niu, F. (2012). Estimating crustal seismic anisotropy with a joint analysis of radial and transverse receiver function data. *Geophysical Journal International*, *188*(1), 144–164. <https://doi.org/10.1111/j.1365-246X.2011.05249.x>
- Long, M. D., & Silver, P. G. (2009). Shear wave splitting and mantle anisotropy: Measurements, interpretations, and new directions. *Surveys in Geophysics*, *30*, 407–461. <https://doi.org/10.1007/s10712-009-9075-1>
- McNamara, D. E., & Owens, T. J. (1993). Azimuthal shear wave velocity anisotropy in the basin and range province using Moho ps converted phases. *Journal of Geophysical Research*, *98*(B7), 12003–12017. <https://doi.org/10.1029/93JB00711>
- Menzies, M., Xu, Y. G., Zhang, H. F., & Fan, W. M. (2007). Integration of geology, geophysics and geochemistry: A key to understanding the North China Craton. *Lithos*, *96*(1–2), 1–21. <https://doi.org/10.1016/j.lithos.2006.09.008>
- Nagaya, M., Oda, H., Akazawa, H., & Ishise, M. (2008). Receiver functions of seismic waves in layered anisotropic media: Application to the estimate of seismic anisotropy. *Bulletin of the Seismological Society of America*, *98*(6), 2990–3006. <https://doi.org/10.1785/0120080130>
- Park, J., & Levin, V. (2016). Anisotropic shear zones revealed by backazimuthal harmonics of teleseismic receiver functions. *Geophysical Journal International*, *207*, 1216–1243. <https://doi.org/10.1093/gji/ggw323>
- Ren, J., Tamaki, K., Li, S., & Junxia, Z. (2002). Late Mesozoic and Cenozoic rifting and its dynamic setting in Eastern China and adjacent areas. *Tectonophysics*, *344*(3–4), 175–205. [https://doi.org/10.1016/S0040-1951\(01\)00271-2](https://doi.org/10.1016/S0040-1951(01)00271-2)
- Rumpker, G., Kaviani, A., & Latifi, K. (2014). Ps-splitting analysis for multilayered anisotropic media by azimuthal stacking and layer stripping. *Geophysical Journal International*, *199*(1), 146–163. <https://doi.org/10.1093/gji/ggu154>
- Silver, P. G. (1996). Seismic anisotropy beneath the continents: Probing the depths of geology. *Annual Review of Earth and Planetary Sciences*, *24*, 385–432. <https://doi.org/10.1146/annurev.earth.24.1.385>
- Silver, P. G., Gao, S. S., Liu, K. H., & the Kaapvaal Seismic Group (2001). Mantle deformation beneath southern Africa. *Geophysical Research Letters*, *28*, 2493–2496. <https://doi.org/10.1029/2000GL012696>
- Smith, W., & Wessel, P. (1990). Gridding with continuous curvature splines in tension. *Geophysics*, *55*(3), 293–305. <https://doi.org/10.1190/1.1442837>
- Song, Z., Zhang, G., Liu, J., Yi, J., & Xue, Y. (2011). Global Earthquake Catalog (in Chinese). Beijing: Seismological Press.
- Sun, Y., Niu, F., Liu, H., Chen, Y., & Liu, J. (2012). Crustal structure and deformation of the SE Tibetan Plateau revealed by receiver function data. *Earth and Planetary Science Letters*, *349–350*, 186–197. <https://doi.org/10.1016/j.epsl.2012.07.007>
- Suo, Y., Li, S., Liu, X., Dai, L., Xu, L., Wang, P., et al. (2013). Structural characteristics of NWW-trending active fault zones in east China: A case study of the Zhangjiakou-Penglai fault zone (in Chinese). *Acta Petrologica Sinica*, *29*(3), 953–966.
- Tao, K., Liu, T., Ning, J., & Niu, F. (2014). Estimating sedimentary and crustal structure using wavefield continuation: Theory, techniques and applications. *Geophysical Journal International*, *197*(1), 443–457. <https://doi.org/10.1093/gji/ggt515>
- Wang, C.-Y., Flesch, L. M., Silver, P. G., Chang, L. J., & Chan, W. W. (2008). Evidence for mechanically coupled lithosphere in Central Asia and resulting implications. *Geology*, *36*(5), 363–366. <https://doi.org/10.1130/G24450A.1>
- Wang, Q., Zhang, P. Z., Freymueller, J. T., Bilham, R., Larson, K. M., Lai, X. A., et al. (2001). Present-day crustal deformation in China constrained by global positioning system measurements. *Science*, *294*(5542), 574–577. <https://doi.org/10.1126/science.1063647>
- Wu, Y., Ding, Z. F., Wang, X., & Zhu, L. P. (2018). Crustal structure and geodynamics of the North China Craton derived from a receiver function analysis of seismic wave data (in Chinese). *Chinese Journal of Geophysics*, *61*(7), 2705–2718. <https://doi.org/10.6038/cjg2018L0244>
- Xu, Y. G. (2007). Diachronous lithospheric thinning of the North China Craton and formation of the Daxin'anling-Taihangshan gravity lineament. *Lithos*, *96*(1), 281–298. <https://doi.org/10.1016/j.lithos.2006.09.013>
- Xu, X. W., Wu, W. M., Zhang, X. K., Ma, S. L., Ma, W. T., Yu, G. H., et al. (2002). New crustal structure motion and earthquake in capital area (in Chinese). Beijing: Science Press.
- Yang, Y., Yao, H. J., Zhang, P., & Chen, L. (2018b). Crustal azimuthal anisotropy in the trans-north China orogen and adjacent regions from receiver functions. *Science China Earth Sciences*, *61*, 903–913. <https://doi.org/10.1007/s11430-017-9209-9>
- Yang, J., Zhao, L., Kaus, B. J. P., Lu, G., Wang, K., & Zhu, R. (2018a). Slab-triggered wet upwellings produce large volumes of melt: Insights into the destruction of the North China Craton. *Tectonophysics*, *746*, 266–279. <https://doi.org/10.1016/j.tecto.2017.04.009>
- Yeck, W. L., Sheehan, A. F., & Schulte-Pelkum, V. (2013). Sequential H-K stacking to obtain accurate crustal thicknesses beneath sedimentary basins. *Bulletin of the Seismological Society of America*, *103*, 2142–2150. <https://doi.org/10.1785/0120120290>
- Yu, Y. Q., Song, J. G., Liu, K. H., & Gao, S. S. (2015). Determining crustal structure beneath seismic stations overlying a low-velocity sedimentary layer using receiver functions. *Journal of Geophysical Research: Solid Earth*, *120*, 3208–3218. <https://doi.org/10.1002/2014JB011610>
- Zelt, B. C., & Ellis, R. M. (1999). Receiver-function studies in the Trans-Hudson orogen, Saskatchewan. *Canadian Journal of Earth Sciences*, *36*, 585–603. <https://doi.org/10.1139/cjes-36-4-585>
- Zhao, B., Gao, Y., & Shi, Y. T. (2013). Relocation of small earthquakes in north China using double difference algorithm (in Chinese). *Earthquake*, *33*(1), 12–21.

- Zhao, B., Gao, Y., Shi, Y. T., Jin, H. L., & Sun, J. (2011). Shear wave splitting in the crust in the intersection zone of the Zhangjiakou-Bohai seismic belt and Shanxi seismic belt (in Chinese). *Chinese Journal of Geophysics*, *54*(6), 1517–1527. <https://doi.org/10.3969/j.issn.0001-5733.2011.06.011>
- Zhao, G. C., Wilde, S. A., Cawood, P. A., & Sun, M. (2001). Archean blocks and their boundaries in the North China Craton: Lithological, geochemical, structural and P-T path constraints and tectonic evolution. *Precambrian Research*, *107*, 45–73.
- Zhao, L., & Xue, M. (2010). Mantle flow pattern and geodynamic cause of the North China Craton reactivation: Evidence from seismic anisotropy. *Geochemistry Geophysics Geosystems*, *11*, Q07010. <https://doi.org/10.1029/2010GC003068>
- Zheng, T., Ding, Z., Ning, J., Chang, L., Wang, X., Kong, F., et al. (2018). Crustal azimuthal anisotropy beneath the southeastern Tibetan Plateau and its geodynamic implications. *Journal of Geophysical Research: Solid Earth*, *123*, 9733–9749. <https://doi.org/10.1029/2018JB015995>
- Zhou, Z. G., & Lei, J. S. (2016). Pn anisotropic tomography and mantle dynamics beneath China. *Physics of the Earth and Planetary Interiors*, *257*, 193–204. <https://doi.org/10.1016/j.pepi.2016.06.005>
- Zhu, R., Chen, L., Wu, F. Y., & Liu, J. L. (2011). Timing, scale and mechanism of the destruction of the North China Craton. *Science China Earth Sciences*, *54*(6), 789–797. <https://doi.org/10.1007/s11430-011-4203-4>
- Zhu, G., Jiang, D., Zhang, B., & Chen, Y. (2012). Destruction of the eastern North China Craton in a backarc setting: Evidence from crustal deformation kinematics. *Gondwana Research*, *22*(1), 86–103. <https://doi.org/10.1016/j.gr.2011.08.005>
- Zhu, R., & Zheng, T. Y. (2009). Destruction geodynamics of the North China Craton and its paleoproterozoic plate tectonics. *Chinese Science Bulletin*, *54*, 3354–3366. <https://doi.org/10.1007/s11434-009-0451-5>